

Electronic band structure and superconducting properties of SnAs

P. I. Bezotosnyi^{1,*}, K. A. Dmitrieva,¹ A. V. Sadakov,¹ K. S. Pervakov,¹ A. V. Muratov,¹ A. S. Usoltsev,^{1,2} A. Yu. Tsvetkov,¹ S. Yu. Gavrilkin,¹ N. S. Pavlov,³ A. A. Slobodchikov,^{3,4} O. Yu. Vilkov,⁵ A. G. Rybkin,^{6,7} I. A. Nekrasov,³ and V. M. Pudalov^{1,8}

¹*V. L. Ginzburg Center for High Tc Superconductivity and Quantum Materials, P. N. Lebedev Physical Institute, Moscow 119991, Russia*

²*Faculty of Physics, National Research University Higher School of Economics, Moscow 101000, Russia*

³*Institute for Electrophysics, Russian Academy of Sciences, Ural Branch, Ekaterinburg, 620016, Russia*

⁴*Kirensky Institute of Physics, Federal Research Center KSC SB RAS, Krasnoyarsk, 660036, Russia*

⁵*Faculty of Physics, Saint Petersburg State University, Saint Petersburg, 198504, Russia*

⁶*Research Park, Saint Petersburg State University, Saint Petersburg, 198504, Russia*

⁷*Laboratory of electronic and spin structure of nanosystems, Saint Petersburg State University, Saint Petersburg, 198504, Russia*

⁸*Quantum Nanoelectronics Laboratory, National Research University Higher School of Economics, Moscow 101000, Russia*



(Received 24 January 2019; published 27 November 2019)

We report a comprehensive study of physical properties of the binary superconductor compound SnAs. The electronic band structure of SnAs was investigated using both angle-resolved photoemission spectroscopy (ARPES) in a wide binding energy range and density functional theory (DFT) within generalized gradient approximation (GGA). The DFT/GGA calculations were done including spin-orbit coupling for both bulk and (111) slab crystal structures. Comparison of the DFT/GGA band dispersions with ARPES data shows that the spectrum for the (111) slab much better describes ARPES data than that for the bulk. In addition, we studied experimentally superconducting properties of SnAs by specific heat, magnetic susceptibility, magnetotransport measurements, and Andreev reflection spectroscopy. Temperature dependencies of the superconducting gap and of the specific heat were found to be well consistent with those expected for the single band BCS superconductors with an isotropic *s*-wave order parameter. Despite spin-orbit coupling present in SnAs, our data show no signatures of a potential unconventional superconductivity, and the characteristic BCS ratio $2\Delta/T_c = 3.48\text{--}3.73$ is very close to the BCS value in the weak coupling limit.

DOI: [10.1103/PhysRevB.100.184514](https://doi.org/10.1103/PhysRevB.100.184514)

I. INTRODUCTION

Binary compounds of the SnX family ($X = \text{Te, Se, As, Sb, P}$) attract much attention due to their unique properties [1–5]. The most extensively studied SnSe [6] and SnTe [7,8] have NaCl structure. These compounds were theoretically and experimentally determined as topological crystalline insulators. In this class of materials topological properties are protected by crystal symmetries, which differs from conventional topological insulators, where the time-reversal symmetry is the determining factor [9]. Moreover, In-doped SnTe was found to manifest signatures of Andreev bound states [10], which are characteristic of unconventional superconductivity. Given this fact and the topological nature of the material, $\text{Sn}_{1-x}\text{In}_x\text{Te}$ is considered as a strong candidate for a topological superconductor [11,12].

Tin arsenide is isostructural to SnTe and SnSe. Without doping, this compound demonstrates superconducting properties, which were first reported in 1964 by Geller and Hull [13]. For a long time there was an uncertainty about the valence state of Sn in this compound and about its possible influence on superconductivity. Later, Wang *et al.* [14] in their experimental studies of polycrystalline SnAs demonstrated that Sn has a single valence state Sn^{+3} . Also, from

rough estimates based on experimental data it was suggested that SnAs is a type-I superconductor with weak coupling. Temperature dependencies of the critical magnetic field H_c and of the specific heat in zero field are well described by the BCS model. Nevertheless, to the best of our knowledge, no information is available on the specific heat behavior in nonzero magnetic fields and on the temperature dependence of the superconducting gap. Furthermore, from earlier theoretical investigations of electronic band structure, electron-phonon interaction, and superconductivity performed in [15], the calculated electron-phonon coupling parameter seemed to agree with the one estimated from specific heat data [14], however, there is a discrepancy between the theoretical and experimental values of T_c .

Another interesting result was found in investigations under high pressure. In Ref. [16] SnAs was shown to exhibit a structural phase transition from NaCl to CsCl structure at around 37 GPa, which confirms previously obtained experimental results [17]. Moreover, there is dramatic increase of T_c up to 12.2 K at a critical point of the structural transition.

On the theoretical side, in Ref. [18] the electronic band structure of SnAs was calculated within the tight-binding approximation. Despite the experimental data of Ref. [14] demonstrating that Sn has a single valence state Sn^{+3} , this compound is considered [18] a potential candidate for the valence-skip material. The valence skipping may lead to a negative effective Coulomb interaction between electrons.

*bezpi@sci.lebedev.ru

The calculation results reveal that the Sn^x state in SnAs is likely intermediate between a valence skipper and fixed valence compound; as a result, moderate charge fluctuations (and electron-phonon interaction) can be responsible for superconductivity.

The band dispersion of SnAs resembles that for SnTe, the known crystalline topological insulator. Moreover, due to the similarity of SnAs to SnTe, it was suggested that the mixed compound $\text{Sn}(\text{As},\text{Te})$ may manifest topological superconductivity, if it is superconducting. Preliminary experimental studies of electronic band structure of SnAs by ARPES technique [19] have shown the presence of features that can be interpreted as a manifestation of the spin-orbit coupling (SOC): Energy band splitting in the vicinity of the Γ point, which might be important in the context of possible topological nature of the mixed compound $\text{Sn}(\text{As}, \text{Te})$. The ARPES data [19] was obtained for the (111) sample surface, whereas band structure calculations are available for bulk dispersion solely. This impedes comparison of the data with theory; obviously one needs band structure calculated for the thin (111) slab rather than bulk.

Despite the existence of previous investigations, there is still a lack of knowledge of the origin of superconductivity in SnAs, and the question about the impact of SOC is still open. In the current paper we report a detailed experimental study of the normal and superconducting properties of SnAs. For the normal state we studied by ARPES technique an electronic band structure in a wide binding energy interval. The measured superconducting properties include specific heat and magnetic susceptibility in various magnetic fields, and the superconducting gap by Andreev reflection spectroscopy. Also, we report refined calculations of the SnAs band structure within DFT/GGA for bulk and (111) slab crystal structures, with and without SOC, and compare them with the ARPES spectra.

II. SAMPLES AND EXPERIMENTAL DETAILS

The single-crystalline SnAs samples were synthesized from pure elements: Sn and As with purity of 99.99% and 99.9999%, respectively. The sealed quartz ampoule with elements taken in a stoichiometric ratio of 1 : 1 was slowly heated to 600 °C, held for 48 h to form the phase, then heated to 800 °C and held for 24 h to homogenize the melt. The crystals were then grown by a modified Bridgman method at a melt cooling rate of 1 °C/h down to 550 °C. The grown crystals were further annealed at a temperature of 550 °C for 24 h to remove growth defects.

We studied two single crystals (No. 1 and No. 2) obtained in two different growths. Being nominally identical, the samples however had slightly different T_c values. For ARPES measurements both SnAs samples were used, for resistance and Andreev spectroscopy we used sample No. 1, for specific heat and magnetic measurements sample No. 2.

The grown SnAs crystals were cleaved into small pieces of about 3 mm size, which had a pyramidal shape with triangular base [Fig. 1(a)]. Structural investigations of both SnAs samples were done with a Rigaku MiniFlex 600 x-ray powder diffractometer. The measured diffraction pattern of SnAs is shown in Fig. 2. It contains only reflexes related to

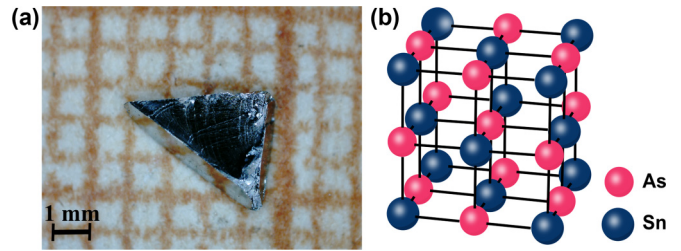


FIG. 1. (a) Image of the SnAs single crystal. (b) Crystal structure of SnAs.

the SnAs phase, and no reflections intrinsic to other phases. From XRD analysis we confirmed the NaCl-type structure [Fig. 1(b)] and found the lattice parameter $a = 5.72483(8)$ Å to be in agreement with earlier reported data [14].

Elemental composition of the sample was measured by EDS (energy-dispersive x-ray spectroscopy) technique using SEM; the spectrum contains only lines related to the Sn and As atoms. Quantitative analysis shows Sn and As content of $48.9 \pm 1.3\%$ and $51.1 \pm 1.3\%$, respectively, which corresponds to the ratio of $(0.978 \pm 0.026) : (1.022 \pm 0.025)$. That is consistent with 1 : 1 composition.

ARPES measurements were performed using a semispherical VG Scienta R4000 energy analyzer with energy resolution of 17 meV and angular resolution of 0.5° . The ultraviolet helium lamp VUV 5k was used as a light source with photon energy 21.2 eV. The measurements were carried out at room temperature. Pressure in the chamber did not exceed $1-2 \times 10^{-10}$ mbar. The samples were cleaved along the (111) plane at room conditions because the single crystal of this material is rather solid and its cleaving in vacuum is difficult. Before measuring photoelectron spectra, the surface of the samples was cleaned by an Ar-ion beam and subsequent heating at temperature of 150 °C under ultrahigh vacuum. The quality of the prepared sample surface was investigated *in situ* by

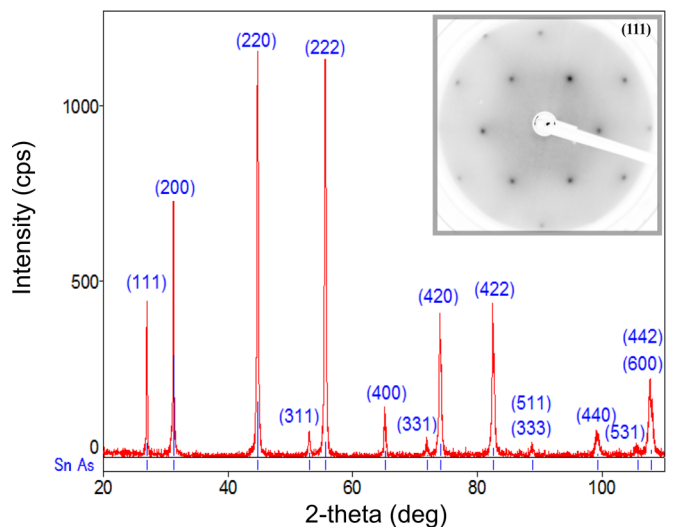


FIG. 2. XRD spectrum of the SnAs (sample No. 2). The abscissa represents the angle 2θ in degrees, the ordinate is the reflection intensity. Inset: LEED pattern for SnAs crystal with electron beam energy $E = 120$ eV.

LEED (low-energy electron diffraction). A regular hexagon with zero reflection at the center in the LEED pattern is shown in Fig. 2 (inset). Since SnAs has the NaCl structure, the obtained pattern of reflections corresponds to the (111) plane, which means the surface restored in a right way after sputtering and annealing. A clear reflection pattern also proves the single phase composition at the investigated surface.

Resistance, magnetic, and thermal properties of the SnAs sample were measured using PPMS-9 (Quantum Design). Specific heat measurements of SnAs crystals were carried out by the thermal relaxation technique with a ^3He calorimeter, in the range of temperatures 0.4–6 K and magnetic fields 0–500 Oe. Low-frequency AC-magnetic susceptibility measurements of SnAs crystals were taken in the range of temperatures 2–6 K and magnetic fields 0–200 Oe. It is worth noting that magnetic susceptibility at “ $H = 0$ ” is actually measured at a finite low value (2–5 Oe) of the AC-magnetic field while the external DC-magnetic field is set to zero. A magnetization loop was measured using a vibrating sample magnetometer (VSM) at a temperature of 2 K. For thermal and magnetic measurements we used a sample with a mass of 6.66 mg.

In order to implement Andreev reflection (AR) spectroscopy, SnS contacts were prepared *in situ* using the break-junction technique [20,21]. In this technique, a flat thin crystal is mounted on a flexible substrate and then is finely bent until it cracks at the preliminary notched narrowing. As a result, a cleft at the designated location is formed in a clean cryogenic environment. After cleaving, using a fine micrometric screw, we adjusted the cryogenic cleavage until a desired Andreev- or Josephson-type I - V characteristic was obtained. During the cryogenic experiment we tuned mechanically the cleavage, and probed, respectively, different microcontacts in order to select a high-transparency contact with the required type I - V characteristic. In order to take four-contact transport measurements the sample was placed on top of the thin printed circuit board (PCB) made of FR-4 textolite; the PCB, in turn, was fixed on a flat Be-bronze springy holder, made of 0.1 mm thick foil. The sample was fixed to PCB with In-clamping contacts, reinforced with silver paste. The springy holder was finely bent by a tip of the micrometric screw pushing the holder from the side opposite to the sample. This design enabled us to cleave the sample and precisely vary the distance between the cleft banks during the cryogenic experiment.

It is a common knowledge that the dI/dV characteristics of high transparency superconductor–normal metal–superconductor (SnS) microcontacts exhibit a so called subharmonic gap structure [22], comprising characteristic dips at bias voltages $V_n = 2\Delta/ne$ with n being the subharmonic number. The subharmonic order n equals the number of Andreev reflections the carriers experience when moving in the normal constriction of the SnS junction. Therefore, the superconducting gap value Δ may be determined directly from the measured V_n versus $1/n$ dependence.

The dI/dV measurements were made in the temperature range from 1.5 to 4 K. The measurements were taken by four probe technique. In order to bias the sample we used a voltage controlled current source fed with a sum of the DC bias and AC modulation voltages. The running current and voltage were measured independently using a precise digitizer; dI and dV were obtained using two lock-in amplifiers SR-830.

III. RESULTS AND DISCUSSION

A. DFT/GGA calculations

A theoretical band structure for SnAs was calculated within density functional theory (DFT) with the full-potential linear augmented plane-wave framework as implemented in WIEN2K [23] together with the generalized gradient approximation (GGA) by Perdew, Burke, and Ernzerhof [24] to the exchange-correlation functional. These calculations were converged self-consistently on a grid of 1000 k points in the irreducible Brillouin zone. Calculations were performed both with and without spin-orbit coupling (SOC). The SOC was considered in a second-variational procedure [25]. Presented below DFT/GGA results for bulk SnAs agree well with those reported earlier in Refs. [15,18].

The DFT calculations for bulk SnAs were based on the space symmetry group $Fm\bar{3}m$ (No. 225) and lattice constant obtained in this work. In order to consider more realistic experimental geometry of the samples we have constructed a (111) slab with a topmost layer of Sn (vacuum gap between slabs is 25 Å). The (111) slab crystal structure is found to have a monoclinic $C2/m$ (No. 12) space symmetry group. Calculations were performed for slabs with thickness of 5 and 2 unit cells (UC). No difference between the band structure was found for 5UC and 2UC slabs. Correspondingly, all discussed below results were obtained for the 2UC (111) slab. Also, we have done structural relaxation for the 2UC SnAs (111) slab, but have not seen any significant atomic position changes. The relaxation causes only minor modification of the electronic structure and is not exploited further.

The DFT/GGA results for SnAs are presented in Fig. 3. Figure 3(a) shows the total, and Figs. 3(b) and 3(c) show partial density of states for bulk SnAs. A mixture of various electronic states (Sn-5s, Sn-5p, and As-4p) is observed near Fermi level with a slight predominance of As-4p states. As a result, the Fermi level lies in the recess of density of states.

SOC impact on the DOS is most pronounced for As-4p states in the interval between -0.5 and -2 eV as follows from Figs. 3(c) and 3(g). Also, SOC slightly affects the Sn-5p states. The same effect is visible for dispersions along X - Γ - L directions in Figs. 3(d) and 3(h). Other bands are practically not affected by SOC. The strongest manifestation of SOC can be observed near Γ point at about -1 eV and provides lifting of the bands degeneracy with the splitting by a few tenths of an eV, in a qualitative agreement with earlier calculations [18,19]. Concerning a possible link between SOC and superconductivity in SnAs, one can see that SOC does not manifest considerably in the vicinity of the Fermi level. Therefore, one should not expect strong influence of SOC on superconductivity.

Several observations based on the DFT/GGA results should be mentioned regarding the superconductivity character in SnAs. First, the bulk DFT/GGA band structure of SnAs [Fig. 3(d)] has many bands crossing the Fermi level with particular Fermi momentum k_F and effective electron mass m^* . Thus, SnAs is a multiband three-dimensional superconductor. This is confirmed by the shape of the calculated Fermi surface presented in Fig. 4 (see also Refs. [16,18]). Second, the total density of states at the Fermi level is rather small,

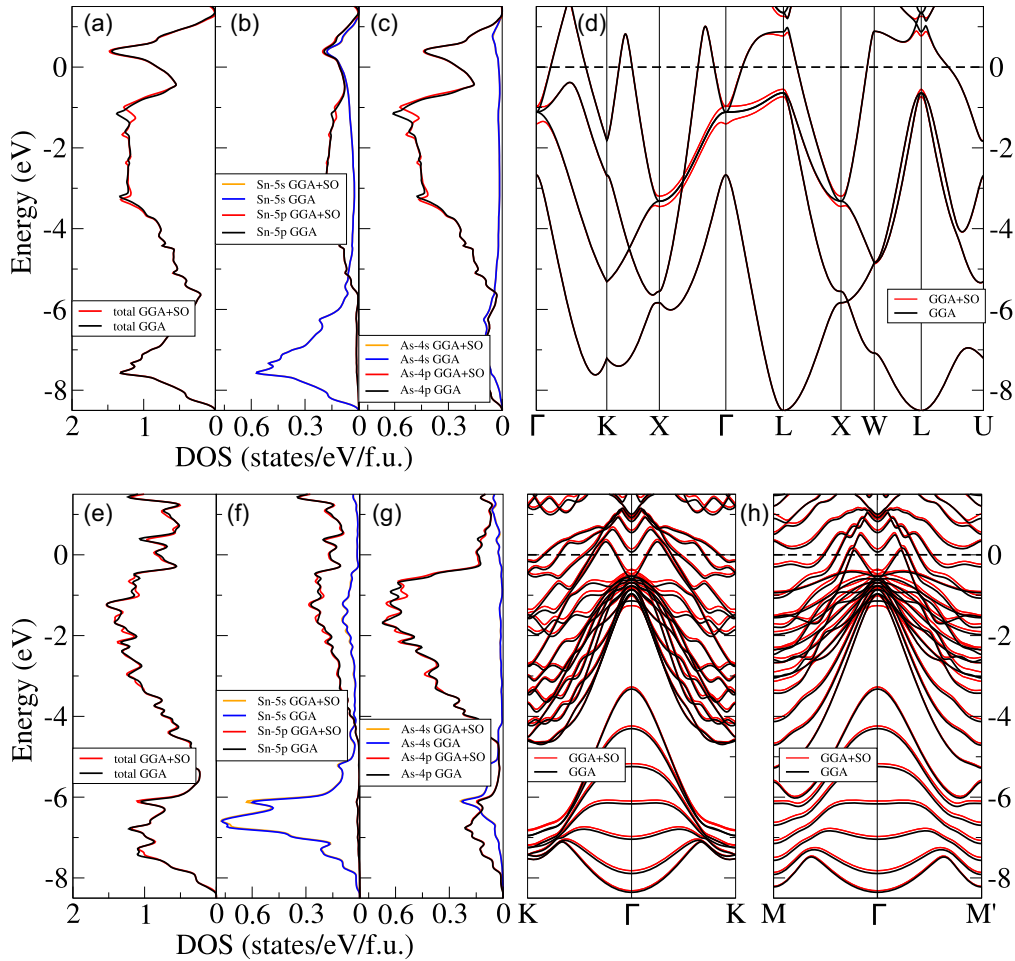


FIG. 3. DFT/GGA calculated total and partial densities of states [(a), (b), (c), (e), (f), (g)] and band dispersions for the bulk (d) and for the slab (h) crystal structures. Positions of high symmetry points in the Brillouin zone are presented in Fig. 5(a). Zero energy corresponds to the Fermi level.

0.81 states/eV/f.u. (f.u. is formula unit) which might lead to experimentally observed low T_c values.

From Figs. 3(d) and 4 one can see that electronic spectra have a complicated anisotropic character.

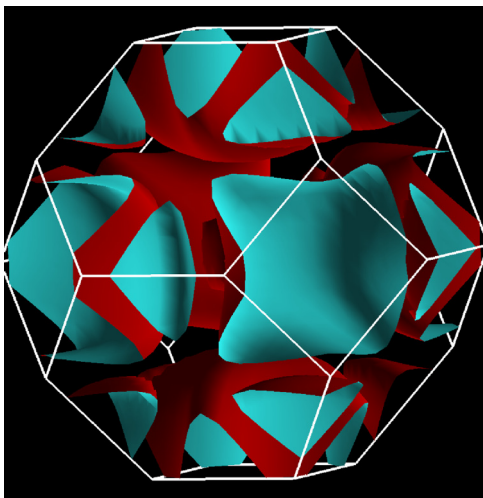


FIG. 4. SnAs DFT/GGA calculated Fermi surface. High symmetry points are labeled in Fig. 5(a).

Since SnAs with a large Fermi surface is a pretty good metal, for further analysis we employ the Fermi liquid type description and deduce from DFT/GGA calculations several parameters important for the superconducting state. First, we estimated the effective mass enhancement through the specific heat linear coefficient $\gamma_{\text{calc}} = \frac{\pi^2}{3} N_A k_B^2 N(E_F) = 1.89 \text{ mJ}/(\text{mol K}^2)$, where N_A is the Avogadro constant, k_B is Boltzmann constant, and $N(E_F)$ is the DFT/GGA value of total DOS at the Fermi level. Then $\frac{\gamma_n}{\gamma_{\text{calc}}} = \frac{m^*}{m_e}$ with $\gamma_n = 2.67 \text{ mJ}/(\text{mol K}^2)$ the electronic specific heat in the normal state (see below) gives $\frac{m^*}{m_e} = 1.41$. This ratio agrees well with Ref. [18] despite both calculated γ_{calc} and experimental γ_n exceed by a factor of ~ 1.2 the respective values used in Ref. [18].

Specific heat, effective mass, and Fermi momentum may be characterized, to the first approximation, with their single values averaged over the Fermi surface despite complicated multiband character of electron dispersions. Finding such averaged parameters for an arbitrary nonelliptic Fermi surface (see Fig. 4) is rather difficult. One can try to obtain k_F value again using $N(E_F)$ the calculated value of the total DOS at the Fermi level. Then $k_F = N(E_F) \frac{4\pi^2 \hbar^2}{V m_e^* m_e} = 0.6 \text{ \AA}^{-1}$, where V is elementary cubic cell volume. Also it may be found

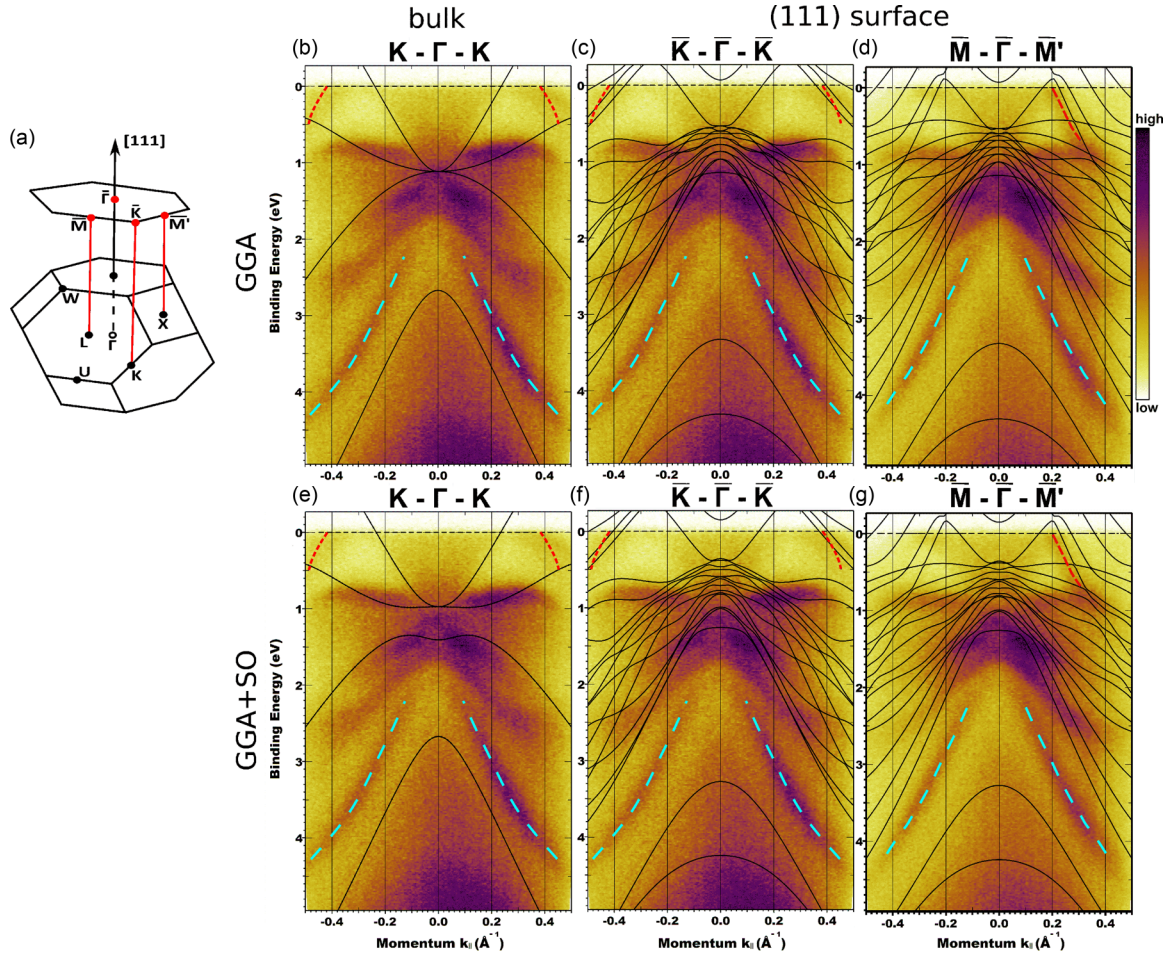


FIG. 5. (a) The first Brillouin zone for the NaCl-type structure with the projection to the (111) plane. (b) and (e) Calculated bulk band structure (solid lines) and ARPES spectra (contour plots) for SnAs along $K-\Gamma-K$ direction. (c), (d), (f), and (g) ARPES spectra with DFT/GGA calculated band structure of the (111) slab along high symmetry directions $\bar{K}-\bar{\Gamma}-\bar{K}$ and $\bar{M}-\bar{\Gamma}-\bar{M}'$ from (a). The lower row corresponds to DFT/GGA calculations with SOC. Dashed lines near the Fermi level show maxima of the ARPES data maps. Zero energy corresponds to the Fermi level.

as $k_F = (3\pi^2 n)^{1/3}$, where $n = N/V$ with N the number of valence electrons in the unit cell. From partial DOS one can see that there are 2.1 As-4*p* electrons, 0.1 Sn-5*s* electrons, and 0.72 Sn-5*p* electrons; hence, in total N per formula unit is 2.92. There are 4 formula units per cubic cell with $V = 187.5 \text{ \AA}^3$. It gives $k_F = 1.23 \text{ \AA}^{-1}$. Such discrepancy between k_F values comes from the multiband anisotropic nature of SnAs spectra, while all definitions above are for the isotropic single-band Fermi liquid. There is also a theoretical conjecture for concentration in Ref. [13] $n = 2.14 \times 10^{22} \text{ cm}^{-3}$, which gives $k_F = 0.86 \text{ \AA}^{-1}$.

Previously these values were estimated in Ref. [14] to be $m^* = 1.20 m_e$ and $k_F = 1.24 \text{ \AA}^{-1}$, respectively, within a straightforward single-sheet spherical Fermi surface approach. Here, from the DFT/GGA calculations we see that the Fermi surface has two sheets and is rather anisotropic. Nevertheless, the values of m^* and k_F obtained here on the basis of DFT/GGA calculations are surprisingly quite similar to those of Ref. [14].

Figures 3(e) to 3(h) present DFT/GGA results for the (111) slab. One can see that the total and partial DOS are practically the same as those for bulk SnAs. The value of

total DOS at the Fermi level also is nearly the same as the bulk one. Manifestations of SOC are weak, however the band dispersions are rather different. First of all, the difference comes from different paths in k space for bulk and (111) slab as shown in Fig. 5(a). Second, there are many more bands for the slab since k_z translation invariance is broken for the surface. As a result, all atoms even of the same sort become inequivalent and produce their own set of bands. Nevertheless, in general SnAs bulk band shape to some extent resembles that for the (111) slab crystal structure.

B. ARPES vs DFT/GGA

Earlier ARPES results obtained by our group were reported in Ref. [19]. We noted there the observed band bundle splitting at the Γ point is not captured by the existing DFT calculations [15,18]. We suggest this disagreement to be caused either by SOC, or by a band structure reconstruction on the crystal surface [19]. We now compare ARPES data and DFT/GGA calculated band dispersions to clarify these issues and conclude that the reason for the band splitting is indeed the reconstruction of the band structure at the crystal surface [19].

Bulk calculations for k_z other than 0 (the k_z direction coincides with the [111] direction) show that by varying k_z it is not possible to improve the agreement between the calculated and experimental spectra, similar to a number of studies [26,27]. In this regard, the work presents the calculation results for the case $k_z = 0$.

Figures 5(b) and 5(e) show ARPES data and DFT/GGA bands for bulk SnAs without and with SOC, respectively. The SnAs bulk DFT/GGA bands resemble ARPES data very remotely. There is a bundle of bands around 1.1 eV (predominantly of As-4*p* character) in calculations and ARPES data. However, DFT/GGA shows only three bands in the bundle, plus one band by 1.5 eV lower, whereas ARPES clearly demonstrates four bands in the vicinity of the Γ point. Also the energy positions of those bands are quite different in ARPES and DFT/GGA. Somehow ARPES does not resolve bands crossing the Fermi level, the most intensive signal is in the vicinity of the Γ point (the momenta interval from -0.2 to 0.2 \AA^{-1} of the ARPES spectra, Fig. 5).

Inclusion of SOC splitting slightly improves the situation. The wings around 0.9 and 1.3 eV agree a bit better with experiment but ARPES does not show clear separation of those bands as calculations suggest. One should note also that bulk DFT/GGA bands along K - Γ - K direction do not reproduce ARPES bands near Fermi level shown by red dashed curves in Figs. 5(b) and 5(e).

In the case of (111) slab calculations, as Figs. 5(c), 5(d), 5(f), and 5(g) show, the calculations demonstrate the emergence of electronic dispersion which much better reproduces ARPES bands near the Fermi level shown with red dashed lines for both \bar{K} - $\bar{\Gamma}$ - \bar{K} and \bar{M} - $\bar{\Gamma}$ - \bar{M} directions. We conclude, the Fermi level crossing positions are well captured by DFT/GGA calculations in the vicinity of the Fermi level. Wings at about 0.9 eV are well reproduced here too. Dark ARPES data region at Γ point about 1.1 eV below E_F is qualitatively represented by a bunch of DFT/GGA “spaghetti.” Strictly speaking not all of these spaghetti may be seen by ARPES since at a given incident beam energy the penetration depth is about 7 \AA . It corresponds to one, maximum two top-most surface layers. The layers below should not contribute significantly to ARPES signal. SOC has almost no effect on the shape of the DFT/GGA bands and does not bring about agreement with ARPES data. Based on the above comparison we conclude that the ARPES spectra in general in the vicinity of E_F are in good agreement with the DFT/GGA calculated bands for the (111) slab of SnAs. However, one band with maximum at about 3 eV (highlighted with light blue dashed curves in Fig. 5) is not reproduced by any of the performed calculations. We believe this feature might be a theme of further studies.

C. Resistance, specific heat, and magnetic susceptibility

In order to get more detailed information about superconducting properties of SnAs we performed resistance, specific heat, and magnetic susceptibility measurements.

To prove the metallic-type conduction in our SnAs samples we present in Fig. 6 a temperature dependence of resistance measured for sample No. 1. Clearly the sample demonstrates metallic behavior despite a low intensity of the branches at

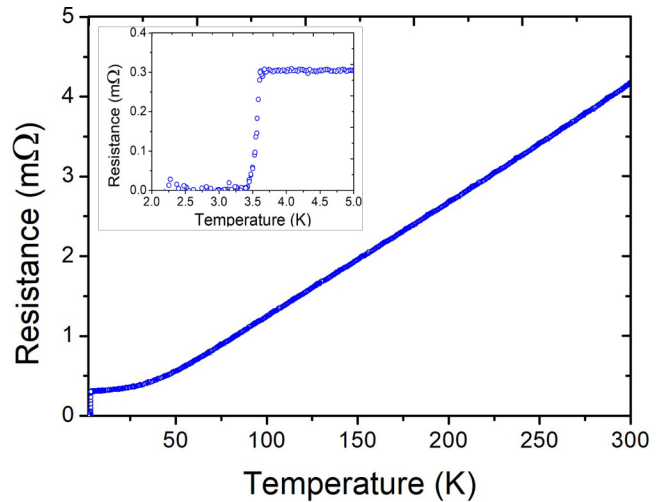


FIG. 6. Temperature dependence of resistance for SnAs (sample No. 1). The inset shows the zoomed-in region of superconducting transition.

the Fermi level in the ARPES data (Fig. 5) and low DOS value in calculations (Fig. 3). At temperature about 3.6 K the resistance shows a transition to the superconducting state (Fig. 6, inset). Metallic behavior and the critical temperature for our single-crystal sample coincide with the previous data [14] for polycrystalline samples. For SnAs polycrystals, more detailed measurements of resistivity in magnetic fields, in superconducting and nonsuperconducting state, as well as temperature dependence of Hall coefficient were carried out by Wang *et al.* [14].

Temperature dependence of the AC-magnetic susceptibility χ of the SnAs crystal is presented in Fig. 7 (for sample No. 2). The susceptibility for this sample demonstrates a superconducting (SC) transition near 3.8 K in zero field, slightly higher than the SC transition in transport (for sample No. 1). As the applied DC magnetic field increases, the superconducting transition temperature gradually decreases and an additional positive peak appears in the $\chi(T)$ dependence

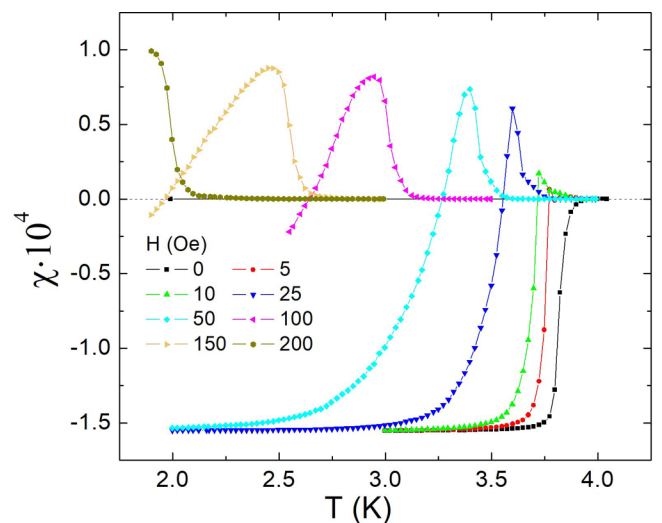


FIG. 7. AC-magnetic susceptibility of the SnAs (sample No. 2) in various DC magnetic fields.

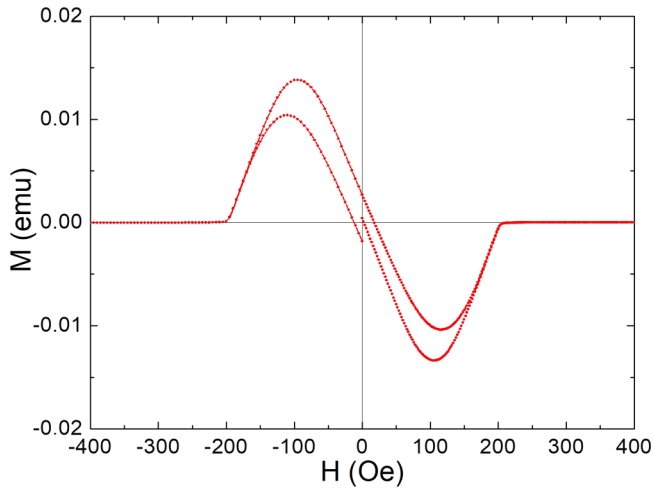


FIG. 8. Isothermal magnetization loop $M(H)$ at 2 K (sample No. 2).

near T_c . This peak corresponds to the so called differential paramagnetic effect (DPE) in superconductors [28–30]. DPE corresponds to the existence of a region with strong growth in $M(H)$ dependence (and, as a consequence, positive derivative $\partial M/\partial H$). This effect is observed for a mixed state of type-I superconductors or in type-II superconductors with close H_{c1} and H_{c2} values.

Figure 8 shows an isothermal magnetization loop $M(H)$ at $T = 2$ K. The shape of the curve is nearly typical for a type-I superconductor, however it reveals a small hysteresis. Such hysteresis is observed in other compounds considered to be type-I superconductors and, generally, is associated with sample shape effects, domain or grain walls, etc. [29,31–34]. More detailed $M(H)$ curves measured at various temperatures close to T_c were also reported in [14]. These curves demonstrate a rapid $M(H)$ drop near H_c in a narrow range of magnetic fields, which is typical both for type-I and for weak type-II superconductors.

Temperature dependencies of the specific heat in various magnetic fields are shown in Fig. 9. The sharp jump in specific heat at $H = 0$ for temperature near 4 K confirms the bulk

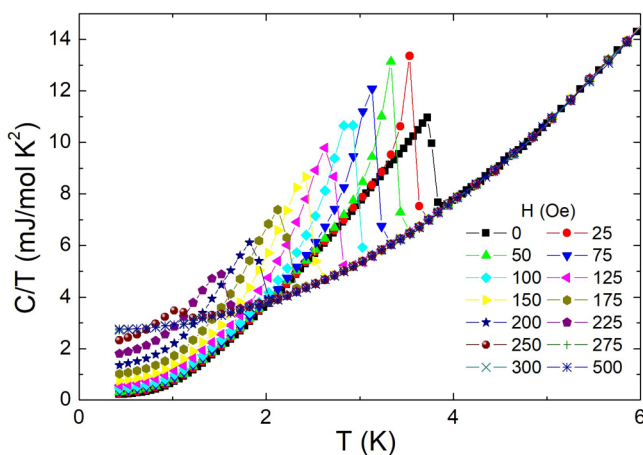


FIG. 9. Temperature dependencies $C(T)/T$ for the SnAs crystal (sample No. 2) in magnetic fields 0–500 Oe.

character of the superconducting transition. This coincides with results in Ref. [14] for specific heat measurements. The bulk-type superconductivity was also consistent with the temperature dependence of χ for zero-field and field-cooling scan modes [14].

From the local entropy conservation we find the critical temperature $T_c = 3.80 \pm 0.05$ K, consistent with susceptibility measurements. The total width of the SC transition $\Delta T_c = 0.15 \pm 0.08$ K is another evidence of the high quality of the studied crystal. In general, our data for zero-field specific heat is reasonably consistent with [14].

Specific heat tends to zero at $T \rightarrow 0$ in zero field and does not demonstrate any anomalies in the low-temperature region. This tendency is an additional evidence of the bulk nature of superconductivity in the studied samples. The polynomial extrapolation to zero temperature $C(T)/T = \beta T^2 + \gamma_r$ [$\beta = 0.32 \pm 0.02$ mJ/(mol K⁴)] gives residual electronic specific heat $\gamma_r = 0.15 \pm 0.03$ mJ/(mol K²).

Magnetic field suppresses the superconducting transition and shifts it gradually to lower temperatures. At fields above 300 Oe, the superconductivity is fully suppressed, as follows from the equality of the specific heat at $H = 300$ Oe and higher fields, for example, 500 Oe. Thus, the electronic component of the specific heat can be defined as $C_e = C(H) - C(H_0) + \gamma_n T$ for $H < H_0$ (where $H_0 = 300$ Oe exceeds the critical magnetic field), taking into account the entropy conservation. The electronic specific heat in the normal state γ_n at temperatures above T_c was found to be $\gamma_n = 2.67 \pm 0.06$ mJ/(mol K²).

The residual term γ_r is much less than the electronic specific heat in the normal state γ_n . The ratio γ_r/γ_n less than 6% quantifies the relative amount of unpaired carriers; it confirms the bulk character of the superconducting state, and evidences for a high crystal purity.

Temperature dependence of the electronic contribution to specific heat $C_e(T)/T$ in various fields is shown in Fig. 10. The inset of Fig. 10 shows the difference between entropy in superconducting and normal states. We now estimate a critical magnetic field value from the obtained data. It could be

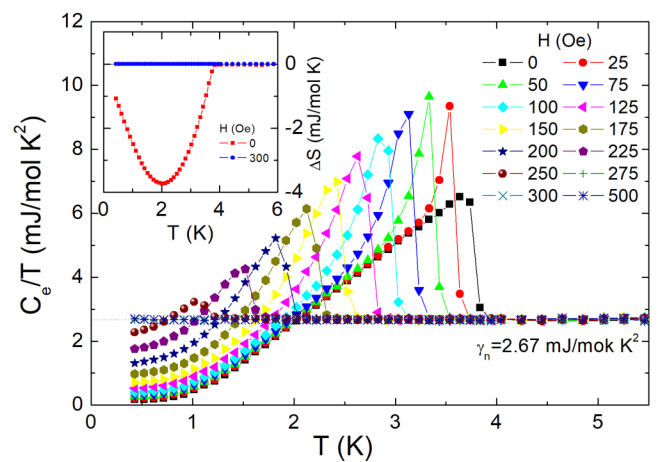


FIG. 10. Electronic specific heat $C_e(T)/T$ in fields 0–500 Oe (sample No. 2). Inset: The difference between the entropy in superconducting state at zero field and normal state (at $H = 300$ Oe) $\Delta S = S_s - S_n$.

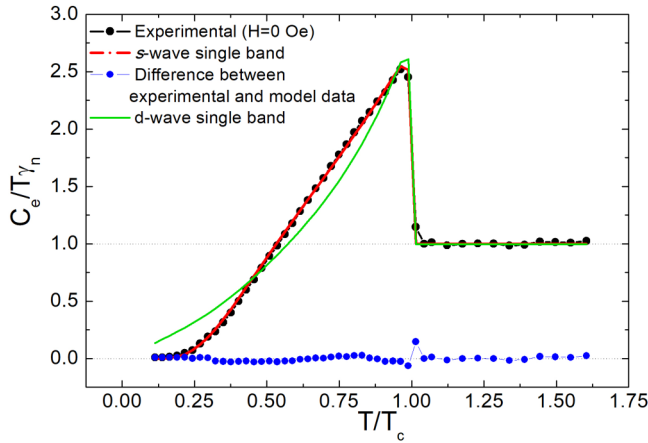


FIG. 11. Normalized electronic specific heat of the superconducting condensate $\frac{C_e}{T\gamma_n}$ and its best fit with the *s*- and *d*-wave α model (sample No. 2).

done from equation $w = \frac{|\Delta F|N}{V} = \frac{H_c^2}{8\pi}$, where w is the density of energy, ΔF is the difference between free energies in superconducting and normal states, N is the molar quantity, and V is the sample volume. Numerical integration gives us $\Delta F = \int_0^{T_c} \Delta S dT = -9.0 \pm 0.2$ mJ/mol, where ΔS is the difference between the entropy in superconducting state at zero field and in normal state. Taking into account $N = m/\mu = (3.440 \pm 0.005) \times 10^{-5}$ mol (here μ is the formula mass of SnAs, $m = 6.66 \pm 0.01$ mg is the sample mass) $V = m/\rho = (0.971 \pm 0.006) \times 10^{-3}$ cm³ ($\rho = 6.86 \pm 0.03$ g/cm³ is the mass density) we have for critical magnetic field $H_c = 283 \pm 10$ Oe.

To analyze thermal properties of superconducting condensate, it is convenient to consider the normalized electronic specific heat $C_{en} = \frac{C_e}{T\gamma_n}$. For the superconducting condensate it may be calculated within the framework of the BCS theory using the so-called α model [35]. The α model may be generalized in case of possible in-plane anisotropy (*d*-wave α model) as presented in [36], with two adjustable parameters $\alpha = \frac{2\Delta(0)}{k_B T_c}$ [$\Delta(0)$ is the superconducting gap at zero temperature], and $m(\varphi) = 1 + \mu \cos(2\varphi)$ is the angular dependence of the gap.

Normalized electronic specific heat of the superconducting condensate $\frac{C_e}{T\gamma_n}$ versus (T/T_c) and its best fit with the *s* and *d* wave α model [35] are presented in Fig. 11. The simplest *s*-wave model [isotropic gap, $m(\varphi) = 1$] has only one free parameter α . The best description of the experimental data was obtained with $\alpha = 3.73$ which is very close to the characteristic BCS ratio ($\alpha = 3.52$) and corresponds to the superconducting gap of $\Delta = 0.6$ meV (see Fig. 11). Clearly the model with the *d*-wave gap symmetry [$m(\varphi) = \cos 2\varphi$] is at odd with the experimental data of Fig. 11. Fitting with the extended *s*-wave gap symmetry [$m(\varphi) = 1 + \mu \cos(2\varphi)$] leads to $\mu \rightarrow 0$, and therefore reduces to the simple *s*-wave model with an isotropic gap. The same result is obtained for the two-band α model which corresponds to the two-band superconductivity [35]: $C(T) = \varphi_1 C_1(T) + \varphi_2 C_2(T)$. In this case from the fitting procedure, the contribution of one of the gaps φ_1 becomes equal to zero, whereas angular modulation for the second one vanishes ($\mu \rightarrow 1$).

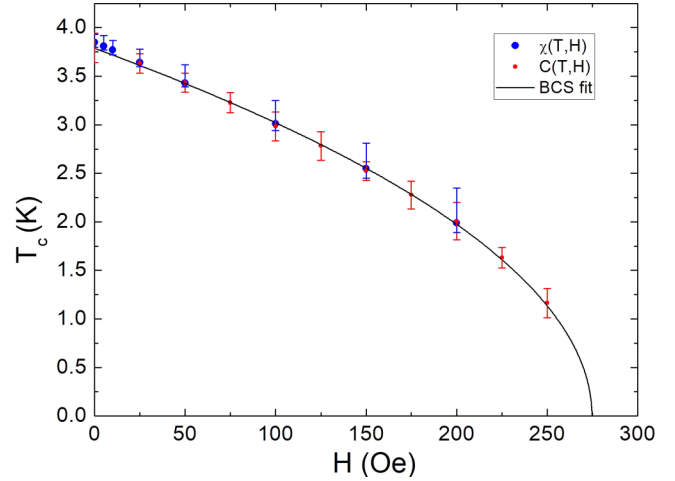


FIG. 12. Critical temperature T_c vs magnetic field, determined from the AC susceptibility and specific heat; solid line represents the BCS parabolic fit $H_c(T) = H_c(0)[1 - (T/T_c)^2]$ (sample No. 2).

Evidently the best description of the experimental data is obtained using the single-band BCS model with an isotropic gap and $\alpha = \frac{2\Delta(0)}{k_B T_c} = 3.71 \pm 0.1$. Despite SnAs as shown above has essentially a multiband electronic system, application of a single-band BCS model can be justified in case the matrix of coupling constant consists of approximately equal values for all Fermi surface sheets [37].

Figures 9 and 10 show temperature dependence of specific heat in magnetic field. Suppression of the specific heat jump at $H = 500$ Oe was also reported in Ref. [14], however, the temperature dependence of specific heat in lower magnetic fields was not explored there. For nonzero fields, beside the conventional jump at $T_c(H)$, the electronic specific heat demonstrates an additional sharp peak near the SC transition (see Figs. 9 and 10). Commonly, such a feature is considered as a transformation of the second- to first-order (in the presence of a magnetic field) phase transition in type-I superconductors, such as, e.g., thallium and aluminum [38,39] as well as for type-I compound superconductors [29,31,33]. The increase in the specific heat near the superconducting transition signifies that an additional energy is required to realize the superconducting transition in magnetic field.

Similar behavior may be also observed for other first-order phase transitions: e.g., for melting transition, where the specific heat of a crystal changes to the specific heat of a liquid right at the melting point, however, the temperature does not change during melting despite the heat entering the system; as a result, the specific heat exhibits a sharp peak. In our case, similarly, the transition from superconducting to normal state occurs with the absorption of latent heat. The finite width of the peak is due to the intermediate state (shape effect). Thus, the specific heat in magnetic fields demonstrates features intrinsic to the first-order phase transition and indicates SnAs to be the type-I superconductor.

Figure 12 shows magnetic field dependence of the superconducting transition temperature, determined from the AC susceptibility and specific heat data. The error bars depict the corridor between the beginning and ending of the transition. The points correspond to the mean values. The mean

$T_c(H)$ data obtained from the specific heat coincides with that obtained from the susceptibility measurements and slightly exceeds the resistance data. This dependence is well described by the BCS dependence $H_c(T) = H_c(0)[1 - (T/T_c)^2]$ that extrapolates to $H_c(0) = 275$ Oe; the latter value is reasonably consistent with $H_c = 283$ Oe, estimated from the difference in entropy between superconducting and normal states. These results differ from those obtained in previous work [14]. The difference may be connected with the single-crystal character of our sample (as compared with polycrystal in Ref. [14]) or with minor difference in the atomic ratio (Sn/As) within uncertainty that was not specified in [14].

The data obtained enables one to estimate superconducting parameters of the SnAs compound. An electronic part of the specific heat in a normal state together with k_F and m^* found from DFT/GGA results described above give us the possibility to estimate London penetration depth λ_L , coherence length ξ , and Ginzburg-Landau parameter κ . For calculations we take DFT/GGA based Fermi momenta k_F from 0.6 to 1.23 \AA^{-1} , while $m^* = 1.41 m_e$ is rather safely obtained from DFT/GGA and specific heat.

Then London penetration depth may be estimated using formula $\lambda_L(0) = (3\pi^2 m^* / [\mu_0 k_F^3 e^2])^{1/2}$. It gives $\lambda_L(0)$ in the range from 25.7 to 75.4 nm. Correspondingly, coherence length $\xi(0) = 0.18 \hbar^2 k_F / (k_B T_c m^*)$ equals 171.0–350.5 nm [40] and Ginzburg-Landau parameter $\kappa = \lambda_L(0) / \xi(0) = 0.07\text{--}0.4 < 1/\sqrt{2}$; the latter confirms our conclusion on the type-I superconductivity for SnAs. For a particular choice $k_F = 1.23 \text{ \AA}^{-1}$, our results are close to those of Ref. [14].

D. Andreev reflections spectroscopy

In order to have a deeper insight into the superconducting properties of SnAs and, particularly, temperature dependence of the superconducting energy gap Δ , we measured Andreev reflection spectra. It is worth noting that in previous work [14] this issue was left unattended. The superconductor-normal metal–superconductor (SnS) Andreev reflection spectroscopy is a powerful tool to determine the energy gap value and its temperature evolution. Unlike several other intimate techniques, such as scanning tunneling spectroscopy (STS), and point-contact Andreev reflections (PCAR), this technique does not require any data fitting [41,42] or a model for data interpreting. Recently, Andreev reflections spectroscopy on symmetric SnS contacts was successfully used to quantify the gap structure for several multigap superconducting arsenides [43–45].

Figure 13(a) shows the dynamic conductance dI/dV of a single Andreev-type contact, measured at $T = 1.5$ K. The two symmetric dips in dI/dV marked with label n_1 in Fig. 13(a) correspond to bias voltages $V_1 = \pm 2\Delta/n_1 e$. No other features are seen at higher bias, and we conclude that the dips correspond to the major $n_1 = 1$ resonance. From this representative data we obtain an estimate $\Delta \approx 0.55$ meV. Andreev reflection dips of higher order may not be seen on this contact due to the following reasons. According to Ref. [42], the number of possible Andreev reflections is limited by the ratio $2a/l$, where a is a characteristic dimension of the constriction and l is the mean free path. Another possible reason is that the second- and higher-order reflection dips may be masked by

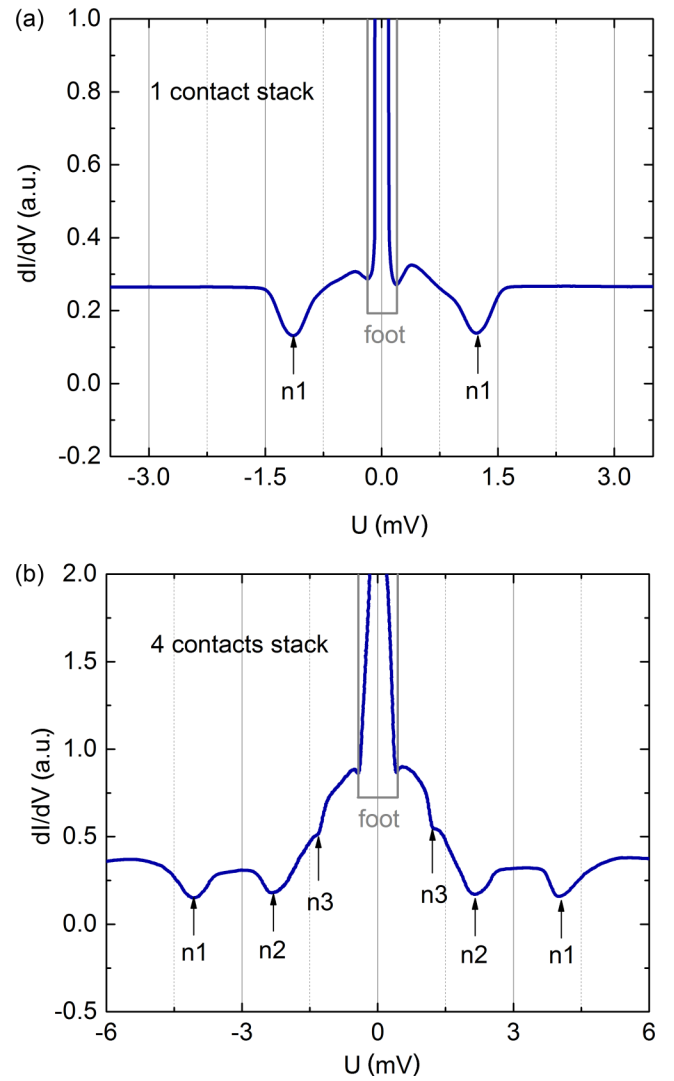


FIG. 13. Dynamic conductances, measured at $T = 1.5$ K for a single SnS contact (a) and for a four-contact stack (b) (sample No. 1).

the sharply growing “foot” (excess conductance at low biases, which is intrinsic to Andreev contacts).

By mechanical tuning the sample bending and thus the break junctions area one can realize Andreev contacts with different $2a/l$ ratio and also stacks of sequentially connected S–n–S–n...–S contacts [20]. For the chain of m contacts, evidently the resonant bias voltage $V_n = m(2\Delta/ne)$ is increased by a factor of m . Figure 13(b) shows a dynamic conductance for such a stack of several contacts. One can see three features, corresponding to three resonances. Having the preceding single-contact spectrum, as a reference, we immediately disentangle the spectrum Fig. 13(b) and find that it is produced by a chain of four sequential contacts. Indeed, the observed dips at 4.1, 2.15, and 1.35 meV may be fitted with $n_1 = 1, n_2 = 2$, and $n_3 = 3$ and the consistency with the single contact spectrum is obtained for $m = 4$. Finally, based on the above data we refine the gap value $\Delta = 0.53 \pm 0.04$ meV and the extrapolated value $\Delta(T \rightarrow 0) = 0.54$ meV. We stress that for all studied contacts we did not observe signatures of the second gap.

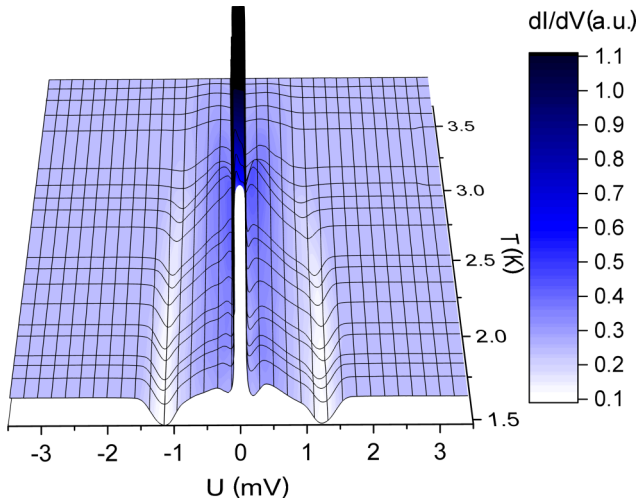


FIG. 14. Temperature evolution of dynamic conductance for a single Andreev contact (the peak at zero bias is cut off).

In order to find $\Delta(T)$ temperature dependence, we measured the dynamic conductance of a single contact in the range 1.5–4 K. Figure 14 shows that with temperature rising, the dips in dI/dV shrink towards zero bias and the dynamic conductance finally linearizes at temperature ≈ 3.6 K, which is taken as the local critical temperature T_c^{local} .

Evolution of the gap value with temperature $\Delta(T)$ is plotted in Fig. 15. One can see that temperature dependence of the energy gap is well approximated by the single-gap BCS theory, and the ratio $2\Delta(0)/k_B T_c = 3.48$ signals the weak-coupling case.

IV. CONCLUSIONS

In summary, we performed comprehensive study of the band structure and superconducting properties of the SnAs

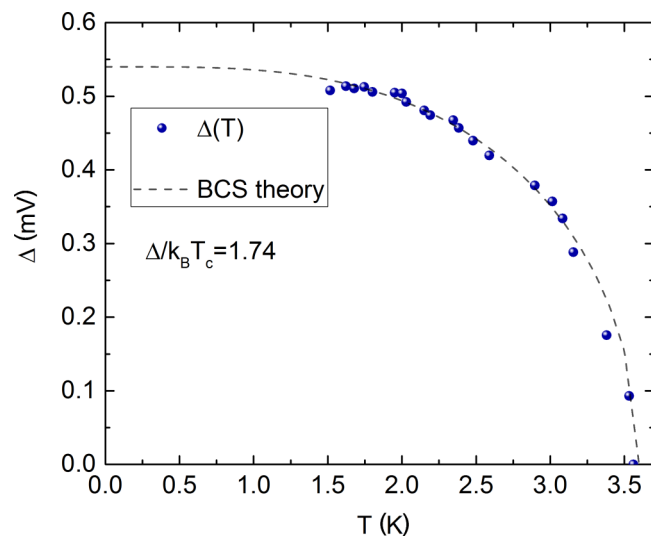


FIG. 15. Energy gap temperature dependence deduced from the measured Andreev spectra. $\Delta = 0.54 \pm 0.04$ meV is found from extrapolation of $\Delta(T)$ to $T = 0$, obtained with the BCS fitting dependence.

binary compound. DFT/GGA band structure calculations were carried out for both bulk and (111) slab crystal structures with and without SOC. Our calculated spectra for bulk SnAs are in a good agreement with previous theoretical results. Experimental investigation of the SnAs band structure was done by ARPES technique. Comparison of the ARPES results and band structure calculation shows that the calculated (111) slab band structure much better agrees with ARPES data than the bulk band structure. SOC does not have a strong influence on the electronic structure of the (111) slab. From our data we deduced quantitative parameters and the type of the superconducting state in SnAs. More specifically,

(i) We confirmed the type-I superconductivity in SnAs by features of the specific heat in nonzero magnetic fields, and by the relationship between the estimated quantitative superconducting parameters.

(ii) We found that the temperature dependencies of critical magnetic field, specific heat jump, and superconducting energy gap are consistent with the conventional weak-coupling BCS model. Our data shows no signature of the unconventional superconductivity, and the superconducting state in SnAs is likely to have the *s*-type symmetry.

(iii) Using two independent techniques (specific heat and Andreev reflection spectroscopy) we determined the superconducting energy gap value $\Delta(0) = 0.61 \pm 0.02$ meV from specific heat data, and $\Delta(0) = 0.53 \pm 0.04$ meV from Andreev reflection spectroscopy. These values also satisfy the weak coupling BCS relationship $2\Delta(0)/T_c = 3.52$.

Table I summarizes our obtained values of the SnAs parameters and compares them with earlier data.

TABLE I. Structural and thermodynamic data for SnAs in the normal and superconducting states. Parameters H_c , γ_r , γ_n , β , and $\Delta(0)$ (specific heat) were obtained for sample No. 2 and $\Delta(0)$ (AR) for sample No. 1. Interval of $2\Delta(0)/T_c$ include parameters for both samples.

Parameters	SnAs single crystal (this work)	SnAs polycrystal (from [14])
a (Å)	5.72483(8)	5.72513(4)
ρ (g/cm ³)	6.86 ± 0.03	–
T_c (K)	3.60 ± 0.15 (sample No. 1) 3.8 ± 0.08 (sample No. 2)	3.58
H_c (Oe)	283 ± 10 (entropy) 275 ± 10 (extrapolation)	178 (extrapolation)
$\Delta(0)$ (meV)	0.61 ± 0.02 (specific heat) 0.53 ± 0.04 (AR)	–
$2\Delta(0)/T_c$	3.48–3.73	–
γ_r [mJ/(mol K ²)]	0.15 ± 0.03	–
γ_n [mJ/(mol K ²)]	2.67 ± 0.06	2.18
β [mJ/(mol K ⁴)]	0.32 ± 0.02	0.30

ACKNOWLEDGMENTS

The authors thank E. Z. Kuchinskii and M. V. Sadovskii for valuable discussions. This work was performed using equipment of the LPI Shared Facility Center and the resource center “Physical methods of surface investigation” (PMSI) of the Research park of Saint Petersburg State University. V.M.P. acknowledges Russian Foundation for Basic Research (RFBR) Grant No. 16-29-03330. P.I.B., K.A.D., A.V.S., K.S.P., A.V.M., A.S.U., A.Y.T., and S.Y.G. were

supported within the state assignment of the Ministry of Science and Higher Education of the Russian Federation (Project No. 0023-2019-0005). A.G.R. acknowledges Saint Petersburg State University for research Grant No. 40990069. I.A.N., A.A.S., and N.S.P. acknowledge Russian Foundation for Basic Research (RFBR) Grants No. 17-02-00015 and No. 19-32-50001, the Program No. 12 of Fundamental Research of the Presidium of RAS. N.S.P. was also supported in part by the President of Russia grant for young scientists No. MK-1683.2019.2.

-
- [1] L.-D. Zhao, S.-H. Lo, Y. Zhang, H. Sun, G. Tan, C. Uher, C. Wolverton, V. P. Dravid, and M. G. Kanatzidis, *Nature (London)* **508**, 373 (2014).
- [2] T. H. Hsieh, H. Lin, J. Liu, W. Duan, A. Bansil, and L. Fu, *Nat. Commun.* **3**, 982 (2012).
- [3] J. Xia, X.-Z. Li, X. Huang, N. Mao, D.-D. Zhu, L. Wang, H. Xu, and X.-M. Meng, *Nanoscale* **8**, 2063 (2016).
- [4] Y. Sun, Z. Zhong, T. Shirakawa, C. Franchini, D. Li, Y. Li, S. Yunoki, and X.-Q. Chen, *Phys. Rev. B* **88**, 235122 (2013).
- [5] M. Kamitani, M. S. Bahramy, T. Nakajima, C. Terakura, D. Hashizume, T. Arima, and Y. Tokura, *Phys. Rev. Lett.* **119**, 207001 (2017).
- [6] Z. Wang, J. Wang, Y. Zang, Q. Zhang, J.-A. Shi, T. Jiang, Y. Gong, C.-L. Song, S.-H. Ji, L.-L. Wang, L. Gu, K. He, W. Duan, X. Ma, X. Chen, and Q.-K. Xue, *Adv. Mater.* **27**, 4150 (2015).
- [7] Y. Tanaka, Z. Ren, T. Sato, K. Nakayama, S. Souma, T. Takahashi, K. Segawa, and Y. Ando, *Nat. Phys.* **8**, 800 (2012).
- [8] Y. Tanaka, T. Shoman, K. Nakayama, S. Souma, T. Sato, T. Takahashi, M. Novak, K. Segawa, and Y. Ando, *Phys. Rev. B* **88**, 235126 (2013).
- [9] L. Fu, *Phys. Rev. Lett.* **106**, 106802 (2011).
- [10] S. Sasaki, Z. Ren, A. A. Taskin, K. Segawa, L. Fu, and Y. Ando, *Phys. Rev. Lett.* **109**, 217004 (2012).
- [11] M. Sato and Y. Ando, *Rep. Prog. Phys.* **80**, 076501 (2017).
- [12] T. Sato, Y. Tanaka, K. Nakayama, S. Souma, T. Takahashi, S. Sasaki, Z. Ren, A. A. Taskin, K. Segawa, and Y. Ando, *Phys. Rev. Lett.* **110**, 206804 (2013).
- [13] S. Geller and G. W. Hull, *Phys. Rev. Lett.* **13**, 127 (1964).
- [14] Y. Wang, H. Sato, Y. Toda, S. Ueda, H. Hiramatsu, and H. Hosono, *Chem. Mater.* **26**, 7209 (2014).
- [15] H. M. Tütüncü and G. P. Srivastava, *Solid State Commun.* **221**, 24 (2015).
- [16] P. V. Sreenivasa Reddy, V. Kanchana, T. E. Millichamp, G. Vaitheeswaran, and S. B. Dugdale, *Physica B: Condens. Matter* **505**, 33 (2017).
- [17] G. B. Demishev, S. S. Kabalkina, T. N. Kolobyanina, T. I. Dyuzheva, and V. G. Losev, *High Press. Res.* **1**, 325 (1989).
- [18] I. Hase, K. Yasutomi, T. Yanagisawa, K. Odagiri, and T. Nishio, *Physica C* **527**, 85 (2016).
- [19] P. I. Bezotosnyi, K. A. Dmitrieva, S. Yu. Gavrilkin, K. S. Pervakov, A. Yu. Tsvetkov, V. P. Martovitski, A. G. Rybkin, and O. Yu. Vilkov, and V. M. Pudalov, *JETP Lett.* **106**, 514 (2017).
- [20] Y. G. Ponomarev, N. B. Brandt, C. S. Khi, S. V. Tchesnokov, E. B. Tsokur, A. V. Varygin, K. T. Yusupov, B. A. Aminov, M. A. Hein, G. Müller, H. Piel, D. Wehler, V. Z. Kresin, K. Rosner, K. Winzer, and T. Wolf, *Phys. Rev. B* **52**, 1352 (1995).
- [21] T. E. Kuzmicheva, S. A. Kuzmichev, M. G. Mikheev, Y. G. Ponomarev, S. N. Tchesnokov, V. M. Pudalov, E. P. Khlybov, and N. D. Zhigadlo, *Phys. Usp.* **57**, 819 (2014).
- [22] M. Octavio, W. J. Skocpol, and M. Tinkham, *Phys. Rev. B* **17**, 159 (1978).
- [23] P. Blaha, K. Schwarz, G. K. H. Madsen, D. Kvasnicka, J. Luitz, R. Laskowski, F. Tran, and L. D. Marks, *An Augmented Plane Wave + Local Orbitals Program for Calculating Crystal Properties* (Techn. Universitt Wien, Austria, 2018).
- [24] J. P. Perdew, K. Burke, and M. Ernzerhof, *Phys. Rev. Lett.* **77**, 3865 (1996).
- [25] D. J. Singh and L. Nordstrom, *Planewaves, Pseudopotentials, and the LAPW Method* (Springer, New York, 2006).
- [26] M. Uruma, A. Sekiyama, H. Fujiwara, M. Yano, H. Fujita, S. Imada, T. Muro, I. A. Nekrasov, Y. Maeno, and S. Suga, *arXiv:0711.2160*.
- [27] A. Damascelli, Z. Hussain, and Z.-X. Shen, *Rev. Mod. Phys.* **75**, 473 (2003).
- [28] R. A. Hein and R. L. Falge, *Phys. Rev.* **123**, 407 (1961).
- [29] L. L. Zhao, S. Lausberg, H. Kim, M. A. Tanatar, M. Brando, R. Prozorov, and E. Morosan, *Phys. Rev. B* **85**, 214526 (2012).
- [30] S. Yonezawa and Y. Maeno, *Phys. Rev. B* **72**, 180504(R) (2005).
- [31] S. Sun, K. Liu, and H. Lei, *J. Phys.: Condens. Matter* **28**, 085701 (2016).
- [32] Y. Yamaguchi, S. Waki, and K. Mitsugi, *J. Phys. Soc. Jpn.* **56**, 419 (1987).
- [33] V. K. Anand, A. D. Hillier, D. T. Adroja, A. M. Strydom, H. Michor, K. A. McEwen, and B. D. Rainford, *Phys. Rev. B* **83**, 064522 (2011).
- [34] V. H. Tran, Z. Bukowski, P. Wisniewski, L. M. Tran, and A. J. Zaleski, *J. Phys.: Condens. Matter* **25**, 155701 (2013).
- [35] F. Bouquet, Y. Wang, R. A. Fisher, D. G. Hinks, J. D. Jorgensen, A. Junod, and N. E. Phillips, *Europhys. Lett.* **56**, 856 (2001).
- [36] A. Muratov, A. Sadakov, S. Gavrilkin, A. Prishchepa, G. Epifanova, D. Chareev, and V. Pudalov, *Physica B: Condens. Matter* **536**, 785 (2018).
- [37] E. Kuchinskii and M. Sadovskii, *Physica C* **470**, S418 (2010), Proceedings of the 9th International Conference on Materials and Mechanisms of Superconductivity.
- [38] A. D. Misener, *Proc. R. Soc. London Ser. A* **174**, 262 (1940).
- [39] D. C. Rorer, H. Meyer, and R. C. Richardson, *Z. Naturforsch. Teil A* **18**, 130 (1963).
- [40] T. P. Orlando, E. J. McNiff, S. Foner, and M. R. Beasley, *Phys. Rev. B* **19**, 4545 (1979).

- [41] R. Kümmel, U. Günsenheimer, and R. Nicosky, *Phys. Rev. B* **42**, 3992 (1990).
- [42] T. Klapwijk, G. Blonder, and M. Tinkham, *Physica B+C* **109-110**, 1657 (1982).
- [43] T. E. Kuzmicheva, A. V. Muratov, S. A. Kuzmichev, A. V. Sadakov, Y. A. Aleshchenko, V. A. Vlasenko, V. P. Martovitsky, K. S. Pervakov, Y. F. Eltsev, and V. M. Pudalov, *Phys. Usp.* **60**, 419 (2017).
- [44] M. Abdel-Hafiez, P. J. Pereira, S. A. Kuzmichev, T. E. Kuzmicheva, V. M. Pudalov, L. Harnagea, A. A. Kordyuk, A. V. Silhanek, V. V. Moshchalkov, B. Shen, H.-H. Wen, A. N. Vasiliev, and X.-J. Chen, *Phys. Rev. B* **90**, 054524 (2014).
- [45] M. Abdel-Hafiez, Y. Zhao, Z. Huang, C.-w. Cho, C. H. Wong, A. Hassen, M. Ohkuma, Y.-W. Fang, B.-J. Pan, Z.-A. Ren, A. Sadakov, A. Usoltsev, V. Pudalov, M. Mito, R. Lortz, C. Krellner, and W. Yang, *Phys. Rev. B* **97**, 134508 (2018).